Remote Sensing of Environment 311 (2024) 114268

Contents lists available at ScienceDirect

Remote Sensing of Environment

journal homepage: www.elsevier.com/locate/rse

Retrieval of snow liquid water content from radiative transfer model, field data and PRISMA satellite data

C. Ravasio [a,*], R. Garzonio [a], B. Di Mauro [b], E. Matta [c,d], C. Giardino [c], M. Pepe [c], E. Cremonese [e], P. Pogliotti [f], C. Marin [g], R. Colombo [a]

[a] Earth and Environmental Sciences Department, University of Milano-Bicocca, Milan, Italy
[b] Institute of Polar Sciences, National Research Council, Milan, Italy
[c] Institute for the Electromagnetic Sensing of the Environment, National Research Council, Milan, Italy
[d] Research Institute for Geo-Hydrological Protection, National Research Council, Turin, Italy
[e] CIMA Research Foundation, Savona, Italy
[f] Climate Change Unit, Environmental Protection Agency of Aosta Valley, Aosta, Italy
[g] EURAC Research, Bolzano, Italy

ARTICLE INFO

Edited by Menghua Wang

Keywords:
Snow water index
Liquid water content
PRISMA images
Alpine area

ABSTRACT

The amount of liquid water (LWC) present in the snowpack is critical for predicting wet snow avalanches, forecasting meltwater release, and assessing water availability in river basins. However, measuring this variable using traditional in situ methods is challenging. Space imaging spectroscopy is emerging as a promising approach to map the spatial and temporal variations of snow parameters. While some studies suggest the potential of hyperspectral remote sensing to infer liquid water content, field validation is still lacking. In this context, we propose a new spectral index, namely Snow Surficial Water Index (SSWI), which is designed to be sensitive to the percentage of surficial liquid water content in snow. We developed the index using the BioSNICAR radiative transfer model and then we tested it on both field spectral data and satellite PRISMA imagery. Validation was performed using field data collected with a Snow Sensor during four campaigns in alpine environments, one of which simultaneously with PRISMA. Through a k-fold cross-validation analysis, we achieved a coefficient of determination of 0.7 and a Root Mean Square Error equal to 3%, demonstrating the effectiveness of the proposed index in retrieving LWC from field data and mapping LWC from PRISMA data. A spatial analysis at the catchment level reinforced the results, showing an LWC distribution consistent with orography. The proposed method can be easily applied to other space imaging spectroscopy missions.

1. Introduction

Understanding the spatial distribution and amount of liquid water (LWC) within a snowpack has substantial implications for snow hydrology and snowpack stability (Conway and Raymond, 1993). LWC plays a critical role in forecasting the start of meltwater runoff and in the effective management of water reservoirs (Brun et al., 1989; Kattelmann and Dozier, 1999). Indeed, the presence of water in snow is an indicator of the snowpack's energy balance and provides information on the timing of snowmelt. Overall, the transition from snow to liquid water is due to the energy inputs to the snowpack from solar radiation, air temperature, or rain-on-snow events (Colombo et al., 2019; Mazurkiewicz et al., 2008). The melting process induces the formation of rounded-shaped grains, and the particle size increases further with each subsequent melt-freeze cycle (Fierz et al., 2009). If during melting the snowpack exhibits <3% water (wet snow), it can rise by capillarity and replace cohesion by sintering. On the contrary, if there is a higher amount of water (above about 8%), it leads to lubrication and fluidization of the snowpack, which might result in discharge and high-density avalanches (Dingman, 2015; Fierz et al., 2009).

The estimation of LWC in snow typically involves field-based measurements for each snow layer. These measurements consist of manually compressing a snow sample and observing its behavior for the presence of liquid water. Different classification schemes can be used and guidelines are provided to ensure the replicability of these tests (Fierz et al., 2009). Nonetheless, the accurate estimation of LWC remains a

* Corresponding author at: Remote Sensing of Environmental Dynamics Lab, DISAT, University of Milano-Bicocca, P.zza della Scienza 1, 20126 Milano, Italy.
E-mail address: claudia.ravasio@unimib.it (C. Ravasio).

https://doi.org/10.1016/j.rse.2024.114268
Received 9 February 2024; Received in revised form 21 May 2024; Accepted 11 June 2024
Available online 20 June 2024

challenging task, even for experienced observers. Overall, the high dynamics in space and time of water flow within the snowpack make these measurements difficult to collect and interpret. Different instruments encompassing various techniques have been hence developed for measuring LWC in the field. The exploitation of the dielectric constant represents the most common approach (Lundberg, 1997). Other techniques include dye tracers (Williams et al., 2010), centrifugal separation (Jones et al., 1983), imaging spectroscopy (Donahue et al., 2022), and freezing, melting, or alcohol calorimetry (Boyne and Fisk, 1987; Fisk, 1986; Kawashima et al., 1998).

Space imaging spectroscopy offers a promising perspective for mapping the spatial and temporal variability of surface parameters related to the cryosphere (Casey et al., 2012; Di Mauro et al., 2017; Engstrom et al., 2022). Different studies have highlighted the possibility to infer snow properties from hyperspectral data gathered from airborne campaigns (e.g., Donahue et al., 2023; Dozier and Painter, 2004; Naegeli et al., 2015; Painter et al., 2013). Current and future spaceborne missions, such as PRISMA (PRecursore IperSpettrale della Missione Applicativa), ENMAP (Environmental Mapping and Analysis Program), CHIME (Copernicus Hyperspectral Imaging Mission for the Environment), SBG (Surface Biology and Geology), and EMIT (Earth surface Mineral dust source InvesTigation), can allow for more systematic and global mapping of snow parameters (Bohn et al., 2022; Di Mauro et al., 2024; Kokhanovsky et al., 2022, 2023; Thompson et al., 2024). In the literature, LWC has been studied and derived from field, airborne, and satellite data using a variety of methods. The first studies by Green et al., 2002, 2006 demonstrated the possibility of inferring LWC from airborne data by exploiting the spectral shift of the reflectance spectra of snow in terms of equivalent absorption path. This method was further used by Dumont et al. (2017) to distinguish between dry and wet snow. Shekhar et al. (2019) introduced a three-band ratio approach method to classify airborne hyperspectral data from AVIRIS (Airborne Visible/Infrared Imaging Spectrometer) into dry and wet snow classes. In recent years, Bohn et al. (2020) developed a retrieval approach to quantify the three phases of water (from Green et al., 2006) using a coupled radiative transfer model based on the Beer-Lambert Law. AVIRIS and PRISMA have been used to map the LWC, given their suitable spectral resolution (Bohn et al., 2021, 2022). These methodologies are based on a simultaneous retrieval of atmospheric and surface parameters using optimal estimation techniques. To incorporate the effect of LWC, the authors used the two-layer coated sphere Lorenz-Mie calculations models of Green et al. (2002). All these studies lack contemporary field validation, and only recently Donahue et al. (2022) performed a laboratory study to retrieve LWC with a Near InfraRed (NIR) hyperspectral camera, providing a validation with independent measurements. Passive microwave remote sensing and synthetic aperture radar (SAR) data also showed promising results in retrieving snow properties. Houtz et al., 2019 proposed a method to retrieve LWC from the L-band radiometer data by using a physically deterministic emission model. Ma et al. (2020) derived the effective snowpack moisture using full-polarimetric SAR data, while Awasthi et al. (2022) proposed a novel modeling approach using hybrid polarimetric datasets. Synergies between different sensors can be pursued in the coming years, exploiting current and future space missions.

In this study, we developed a remote sensing approach to obtain the spatial distribution of LWC in surficial snow. The objective of this study is the development and application of a hyperspectral index sensitive to LWC variations in surficial snow. The spectral index has been developed using simulations from the BioSNICAR radiative transfer model (Cook et al., 2020) and then tested on both field and PRISMA spectral data. Performance validation has been conducted using field data of LWC collected by the Snow Sensor (FPGA Company, 2018) in four field campaigns carried out over snow covered areas in the Italian Alps.

2. Data and methods

2.1. Study sites and ground-based data

Field data of snow parameters and optical properties were collected in four campaigns at the following sites of the Italian Alps: Plateau Rosa, Laghi Cime Bianche, Formazza, and Stelvio (Fig. 1).

Table 1 summarizes the site locations, the main characteristics of the snowpack, and the different measurements. Overall, a total of 52 LWC measurements were collected with LWC ranging from 0 to 15% and snow density from 250 to 411 kg/m^3. The LWC measurements were taken using a Snow Sensor, a capacitance sensor that assesses the relative permittivity when placed on the snow (SLF Snow Sensor, FPGA Company, 2018). The instrument can measure snow moisture that ranges from 0 to 20 and directly provides LWC measurements in percentage units (of volume). LWC measurements were replicated three times at each point. The Snow Sensor requires the value of the dry snow density, which can be critical to know. In this work, we assumed the dry density as the first measurement of density in the morning, as suggested by the instrument manufacturers. The penetration of the electric field of the Snow Sensor into the snow is about 17 mm (Donahue et al., 2022). LWC measurements at Plateau Rosa were performed on the glacier covered by seasonal snow in a warm summer condition. The LWC data at Stelvio have been collected on the glacier tongue some days after an early snowfall event, when warm air temperatures forced the melting of the snow during the day, changing the LWC.

Table 1 also shows information about the field spectroscopy measurements and satellite data availability, which are fully described in Section 2.3. The campaign at Laghi Cime Bianche was conducted on the 21st of February 2023, quasi-simultaneously with a PRISMA overpass at 11.00 UTC. The PRISMA image covers an area of 30 by 30 km (cf. Fig. 1). We conducted LWC measurements in 9 different areas of about 30 m × 30 m each (consistent with the PRISMA spatial resolution of 30 m). In 3 of these areas, we also performed reflectance measurements.

2.2. LWC modeling with BioSNICAR

2.2.1. Model setting

The spectral complex refractive index of ice (Picard et al., 2016; Warren and Brandt, 2008) and of water (Segelstein, 1981) are shown in

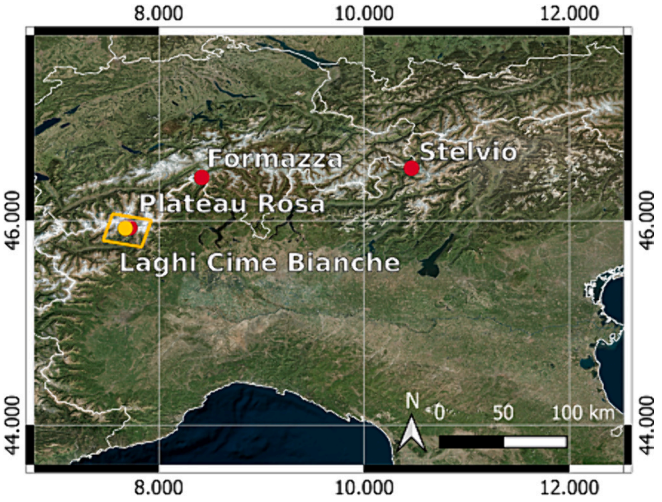

Fig. 1. Investigated areas (Plateau Rosa, Formazza, and Stelvio) are depicted as red points. The yellow rectangle shows the area covered by the PRISMA satellite image. The campaign at the Laghi Cime Bianche site was conducted simultaneously with the PRISMA overpass, and it is depicted as a yellow point. (For interpretation of the references to colour in this figure legend, the reader is referred to the web version of this article.)

Table 1
Information about study areas, snow characteristics, field spectral measurements and satellite PRISMA data availability.

Site name	Sites location (Lat; Lon)	Elevation (m asl)	Campaign date	LWC sampling sites	LWC range (%)	Mean snow density (kg/m^3)	Mean SSA (m^2/kg)	Field spectroscopy points	PRISMA image
Plateau Rosa	45.930003°; 7.681924°	3500	30/06/2021	8	0–9.1	411 ± 40	14.0 ± 0.4	8	NO
Stelvio	46.514032°; 10.459534°	2561	18/10/2022	16	0.4–14.48	200 ± 60	15.0 ± 4.0	16	NO
Laghi Cime Bianche	45.933883°; 7.713678°	2810	21/02/2023	9	0–9.2	350 ± 69	12.4 ± 3.9	3	YES
Formazza	46.423439°; 8.415994°	1700	03/03/2023	19	0–10.1	250 ± 50	18.0 ± 3.8	19	NO

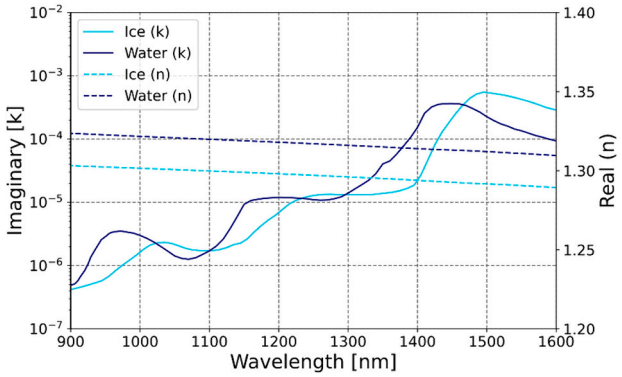

Fig. 2. Real (dashed line) and imaginary components (continuous line) of the refractive index of ice (light blue line) and water (blue line). (For interpretation of the references to colour in this figure legend, the reader is referred to the web version of this article.)

Fig. 2. Of the various properties of snow, the surficial liquid water content and the grain size affect the snow reflectance over a wide spectral range, from 800 to 2500 nm (Warren, 1982). Across this spectral range, the imaginary component of the refractive index of both ice and water varies significantly and contains several local minima that are shifted relative to each other. As a result of this shift, there are also differences in the reflectance spectrum of dry and wet snow (Green et al., 2002).

The BioSNICAR radiative transfer model (Cook et al., 2020; Flanner et al., 2007) was used to evaluate the sensibility of surficial LWC to reflectance and to develop a new spectral index sensitive to LWC variations. The rationale for building the spectral index from a physical model is that since the reflectance is affected by the physical properties of the snow, these can be predicted by establishing a functional relationship between snow properties and surface spectral reflectance. The BioSNICAR simulates the Bi-Hemispherical Reflectance Factor (BHRF, Schaepman-Strub et al., 2006) with a two-stream approach (Flanner et al., 2021) in a wide spectral range, from ultraviolet (200 nm) to mid-wave infrared (5000 nm), with a resolution of 10 nm. The model inputs include the illumination conditions (e.g., solar zenith angle - SZA - and the atmospheric profile from seven different locations on the Earth), the snow layer structure (e.g., number and thickness of layers, density, grain size, and LWC), and the type and the concentration of organic/inorganic impurities externally mixed with the snow or ice. In this model, the snow is represented as a bulk medium of air with discrete grains represented as spheres. We used the Mie theory since the melting process induces the formation of round grains (Fierz et al., 2009). During periods of high radiation and near-freezing temperatures (as in our study), small ice grains likely melt from their surface, forming water-coated grains or clusters of well-rounded grains. Therefore, we simulated the interstitial melt water as liquid water coatings around ice grains (Green et al., 2002), although different conditions exist, as described in Colbeck (1980); Donahue et al. (2022).

Under these assumptions, we modeled the snowpack as two layers (5 cm and 60 cm in depth, respectively), where only in the first one LWC is generated and produced. This approach should allow to be consistent with field spectral data. The simulation of spectral data was performed at the BioSNICAR spectral resolution of 10 nm. We created a library of 1743 reflectance simulations, varying the grain size values from 100 to 1450 μm by 25 μm steps, the SZA from 20 to 70° by 10° steps, and the LWC values from 0 to 20% by 1% steps. To better represent the snowpack conditions, we set the density values according to LWC values as follows: 300 kg/m^3 for LWC values ranging from 0 to 4%, 350 kg/m^3 from 5 to 9%, 400 kg/m^3 from 10 to 14%, and 450 kg/m^3 from 14 to 20%, respectively. As for the other parameters available in the model, we used direct solar radiation and a mid-latitude winter atmosphere. Since the light absorbing particles (LAPs) present in the snowpack affect the spectral reflectance (e.g., Di Mauro et al., 2021), we performed BioSNICAR simulations by increasing the volumetric concentration of black carbon (from 100 to 1000 ppb by 100 ppb step) and Saharan dust particles (from 100 to 1000 ppm by 100 ppm step) with varying LWC from 0 to 20%. As the organic impurities in the snowpack affect the spectral reflectance only in the visible range (400–785 nm) (Di Mauro et al., 2021), which lies outside the considered absorption feature, we decided to exclude them from the simulations.

An example of simulated data for different grain sizes and LWC is shown in Fig. 3. Fig. 3a shows the snow reflectance with variable snow grain size. The transition may mimic from pristine snow (grain effective radius of about 50 μm) to aged snow (about 1500 μm), and it produces a decrease of reflectance mainly in near-infrared wavelengths, without any shift or shape deformation of the absorption feature at 1030 nm. The reason is that large-coarse grains exhibit higher absorptive and forward scattering properties compared to fine grains due to the longer light path within the ice crystal, resulting in increasing light absorption (Wiscombe and Warren, 1980). Different methods have been developed and successfully tested for deriving grain size from multispectral and hyperspectral data (Dumont et al., 2017; Garzonio et al., 2018; Kokhanovsky et al., 2019; Negi and Kokhanovsky, 2011; Nolin and Dozier, 2000). Fig. 3b shows the reflectance with increasing values of surficial LWC and grain size equal to 500 μm. During the snow melting season in alpine catchments, an increase in the effective grain size generally occurs when liquid water fills the gaps between ice grains, leading the refractive index of the moist ice to align with that of water. Green et al. (2002) first highlighted that the position of the local minimum corresponding to the absorption feature at 1030 nm shifts toward lower wavelengths with increasing LWC, in particular in the spectral range between 800 and 2500 nm. The magnitude of this shift is about 20 nm in the 0–20% LWC range. The effect of the LWC on reflectance is less than the effect of the grain size on reflectance but can affect grain size retrieval if not accounted for (Donahue et al., 2022).

2.2.2. *Spectral index development*

To analyze in detail the spectral feature centered at 1030 nm, and to decouple the effects of grain size, SZA, and LWC in the detected signal, we propose an approach based on the development of a new spectral index. Firstly, we applied a Continuum Removal (CR) approach within

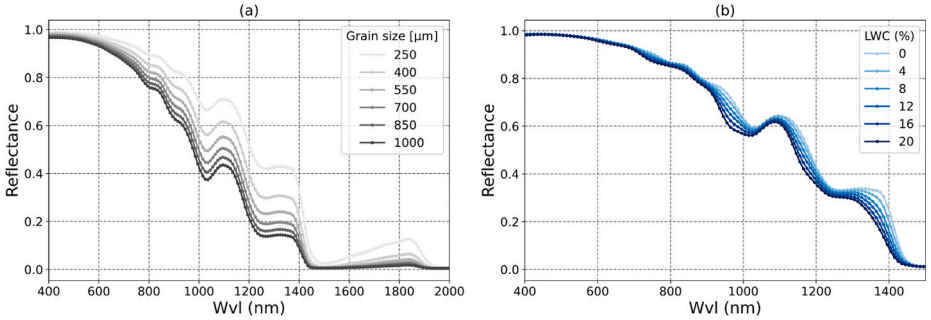

Fig. 3. (a) Modeled dry snow reflectance for grain size ranging from 100 to 1000 μm; SZA = 50°. (b) Modeled snow reflectance for grain size = 500 μm with LWC ranging from 0 to 20%; SZA = 50°.

the absorption feature considering the method proposed by Clark and Roush (1984). This technique involves establishing a convex continuum between two anchor points of the reflectance in the referred wavelength range and then subtracting it. Here, we have considered the CR between 905 and 1125 nm as band shoulders. Among the advantages of using the CR method, the estimation of LWC is expected to be independent of the absolute magnitude of spectral reflectance (Nolin and Dozier, 2000). Subsequently, the continuum-removed spectra were fitted with a Gaussian function (Pepe et al., 2023). Fig. 4 shows two examples of the continuum removal with different LWC values for two typical snow grain sizes (Fig. 4a, grain size = 400 μm; Fig. 4b, grain size = 800 μm). For higher LWC values, the minimum in the snow spectra is clearly shifted to shorter wavelengths and the area becomes asymmetric. We found that the magnitude of the spectral shift after the application of the CR method is about 27 nm for a 20% change in LWC. This value is dependent on the position of the anchor points of the CR. In the presence of dry snow (for LWC = 0), the CR is centered around 1025 nm, and it shows increasing depths with increasing grain size (Fig. 4a and b). The depth of the absorption features at 1025 nm (d_{dry}) can be exploited to modulate the grain size variability and to minimize its effect on the recorded signal.

This analysis allowed us to introduce the dimensionless Snow Surficial Water Index (SSWI), which is defined as the semi-area of the absorption feature normalized to d_{dry} as:

$$SSWI = \frac{1}{d_{dry}} A_{1025} = \frac{1}{d_{dry}} \int_{\lambda=905}^{\lambda=1025} \frac{R_c(\lambda) - R(\lambda)}{R_c(\lambda)} d\lambda \quad (1)$$

where R_c is the continuum reflectance, and R is the reflectance; A_{1025} is the semi-area, which is estimated by numerical integration with the trapezoidal rule between the anchor points of the CR feature at 905 nm and 1025 nm, inspired by the Nolin and Dozier (2000) approach. The choice to use a semi-area rather than the whole area of the absorption feature is due to a fine tuning of the standard deviation when considering the grain size variability. A_{1025} increases exponentially with the grain size and d_{dry} also increases with grain size with the same exponential law (data not shown). Similarly, A_{1025} and d_{dry} decrease with the SZA with the same exponential law. Therefore, we expect SSWI to be independent of both grain size and SZA. Moreover, SSWI is independent from impurities in the scenario of low LAPs concentration (<0.6 ppm for carbonaceous particles and < 500 ppm for dust, data not shown), and it can be therefore applied only under this condition. This index relates very well to the method presented by Green et al., 2002 (with a determination coefficient R^2 of 0.994, data not shown).

Under the Lambertian assumptions, we developed SSWI from BHRF simulations from BioSNICAR, and then we applied it to the Hemispherical-Conical Reflectance Factor (HCRF) spectra derived from field measurements and PRISMA image. Other studies used the same approach (Chevrollier et al., 2022; Di Mauro et al., 2017, 2024; Kokhanovsky et al., 2019). However, the Lambertian assumption may introduce some uncertainty in SSWI and LWC retrievals, but this analysis was beyond the scope of this study.

The performance of SSWI to derive LWC was evaluated by using both simulated and measured datasets and then tested in a regression model with both field measurements and PRISMA images to retrieve LWC from observed data.

2.3. Field spectroscopy, PRISMA satellite data preprocessing and statistical analysis

Field spectroscopy measurements were performed at the same time as LWC, snow density, and specific surface area measurements at each investigated site. All the measurements were performed on clear sky days on almost flat terrain (<5°) and clean snow conditions (no visible layers of impurities). Spectral measurements were conducted using a Spectral Evolution (SR-3500) full range portable spectroradiometer (spectral range from 350 nm to 2500 nm; spectral resolution ≤3.5 nm from 350 to 1000 nm, ≤ 10 nm from 1000 to 1900 nm, and ≤ 7 nm from 2100 to 2500 nm).

The measured reflected radiances, replicated three times for each site, were converted into reflectance (namely HCRF) by normalizing the reflected radiances measured over snow targets with the radiances reflected from a calibrated Lambertian Spectralon panel. Data at the native spectral resolution were resampled to 10 nm to be consistent with the spectral setting of both BioSNICAR and PRISMA. During the campaign at Laghi Cime Bianche, reflectance measurements were collected in 3 different areas, with 20 measurements in each area, where LWC measurements were also performed (Section 2.1).

The level 1 - top-of-atmosphere radiance (L1) - PRISMA standard products were downloaded from the PRISMA portal and pre-processed using the *prismaread*[1] tool (Busetto and Ranghetti, 2020) to convert the PRISMA data package into a single hyperspectral data-cube from the Visible – Near-InfraRed (VNIR) to Short Wave InfraRed (SWIR) region. To ensure a precise geolocation with the field measurements, a geocoding process was performed. Using *prismaread*, a primary bow-tie correction, gap filling, and gridding in geographic coordinates are performed. Then, a Python script based on the AROSICS package,[2] was used to perform automatic subpixel co-registration of PRISMA (GSD 30 m) with Sentinel 2 data (GSD 20 m) as a reference. The AROSICS algorithm (Scheffler et al., 2017) applies an improved phase-correlation approach employing a discrete Fourier transformation domain to derive pixel geometrical displacement of the slave PRISMA image with respect to the Sentinel-2 master image (chosen as close as possible to the PRISMA overpass). The local co-registration algorithm option was used for extracting tie-points toward a moving window across a 10-m grid of control points. Since the algorithm runs for single monochromatic image

[1] https://irea-cnr-mi.github.io/prismaread/index.html.
[2] https://www.gfz-potsdam.de/en/software/automatic-subpixel-co-registration-geomultisens.

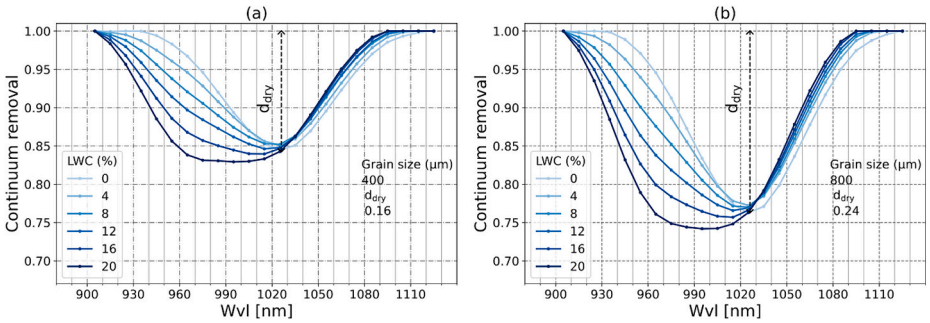

Fig. 4. Example of a continuum removal (CR) around the absorption feature at 1030 nm with varying LWC. The grain sizes used for the simulations are 400 μm (a) and 800 μm (b). The center of the CR for LWC = 0 is located at 1025 nm, and its depth (d_{dry}) increases with the grain size.

pairs, PRISMA band 51 was paired with Sentinel-2 band 8. Afterwards, AROSICS was used to extract tie-points, while their altitude was extracted from a Digital Elevation Model (DEM) and included in the final ortho-projection by second order polynomial transformation in GDAL. Residual errors are around half-pixel size.

The entire process results in a geocoded L1 hypercube with 30 m spatial resolution. Geocoded L1 data were then corrected for atmospheric effects with the ATCOR3 software (Richter, 1998). The rugged terrain mode was used, ingesting elevation data from the local DEM for atmospheric altitude compensation. A rural aerosol type was used, and water vapor in the atmosphere was set to vary spatially, using the atmospherically pre-corrected differential absorption (APDA) method (Schläpfer et al., 1998, implemented in ATCOR3) applied at the 820 nm water absorption region. The atmospheric visibility was set to 23 km (as modeled by ATCOR3 and consistent with the Aerosol Optical Depth provided within the PRISMA standard product), while the range of adjacency effect was set to 1 km.

Finally, to reduce the noise in the ATCOR3-derived PRISMA reflectance we applied a Savitzky-Golay smoothing filter (kernel = 6 and polynomial order = 3). This smoothing preserves the signal within the investigated absorption feature at 1030 nm, where the PRISMA spectral bandwidth of 12.95 nm is also comparable to the 10 nm bandwidth of both the BioSNICAR simulations and the SR-3500 field data. The smoothed ATCOR3-derived PRISMA image of reflectance allowed the continuous shape of the absorption spectra within the spectral region used by the SSWI.

To obtain a snow cover map, we exploited a modified version of the Normalized Difference Snow Index (NDSI) (Dozier, 1989) on the smoothed PRISMA reflectance image. Since the NDSI was originally designed for multispectral data (Hall and Riggs, 1995), we adopted the NDSI formulation proposed for the Hyperion satellite sensor (Negi et al., 2013) considering 500 nm and 1600 nm. According to the literature, where NDSI is >0.4 the surface is largely covered by snow.

We finally computed the SSWI index both on field data and PRISMA image according to Eq. (1). The SSWI from PRISMA have been calculated by averaging the reflectance of regions of interest corresponding to a window of 3 × 3 PRISMA pixels centered on the 9 sites where the LWC measurements were measured. Field and PRISMA derived SSWIs were analyzed together since for PRISMA we had only 9 matchups. The empirical relationship between SSWI and manually measured LWC was established using inverse Ordinary Least Squares (OLS) regression techniques and evaluated in terms of R^2 and RMSE. The OLS technique allowed us to calibrate the inverse form of the empirical relationship. In particular, we employed the measured LWC variable as the predictor and SSWI as the dependent variable to estimate the OLS coefficients. The validation of the OLS model was performed with the k-fold approach splitting the dataset into five subsets (number of samples = 11). The model was fitted using four subsets for the training, and the validation was performed using the remaining subset. We repeated the k-fold cross-validation to improve the estimated performance, involving 15 multiple iterations of the procedure. The performance of the model was evaluated in terms of cross-validated coefficient of determination (R^2_{CV}) and cross-validated root mean square error ($RMSE_{CV}$). The inverse model was finally applied to the PRISMA snow cover map to produce the LWC map in the Laghi Cime Bianche area. From PRISMA data we excluded the snow shaded areas by imposing a threshold on the blue reflectance (i.e. $\rho_{497} > 0.4$) since the application of the CR approach produced unreliable values (LWC >20%). The LWC map was finally interpreted by considering spatial patterns according to aspect and altitude in different catchments derived from the DEM of the Aosta Valley (Italy).

3. Results and discussion

3.1. SSWI performance on simulated data

Fig. 5a and b show the average trend of the SSWI computed according to Eq. (1) over the SZA (0–70° range) and grain size (250–1450 μm range) respectively, while Fig. 5c shows the behavior of SSWI with regards to LWC. The SSWI is almost independent of the SZA and grain size, and it is significantly linearly correlated with LWC in the case of Lambertian surfaces and low LAPs values. Therefore, these simulations appear to suggest that this spectral index can minimize grain size and SZA effects and therefore to maximize sensitivity to liquid water content.

Other methods to retrieve LWC have been proposed in the literature and these can present advantages over the proposed method. The full retrieval of snow parameters from space presented in Bohn et al. (2022) allows for consistent estimates of snow parameters and it may represent the state of the art, although model parameterization and inversion approaches imply a significant complexity. Such approaches allow the estimation of LWC in the predictive mode, therefore overcoming the need for parameterization required for the use of regressive empirical models. In this study, we focused on a single snow parameter that can be estimated by a spectral index using an empirical approach. SSWI is easy to implement: it can be computed from different space imaging spectroscopy, and it can be considered as a proxy for LWC to investigate its spatial and temporal patterns. A full comparison of different methods, an uncertainty analysis and a full validation scheme with real data are currently missing and should be pursued with the advent of new space imaging spectroscopy missions.

3.2. LWC retrieval from field spectroscopy and PRISMA image

Fig. 6 shows the field SR-3500 reflectance spectra and the corresponding CR spectra at each of the investigated Alpine sites (cf. Fig. 1). The variability observed in the CR analysis can be mostly explained by the change in snow properties since impacts due to the SZA and grain size are suppressed by this method. The spectral shift of the minimum absorption is clearly visible in Fig. 6b at the Stelvio site, where we recorded the widest LWC range.

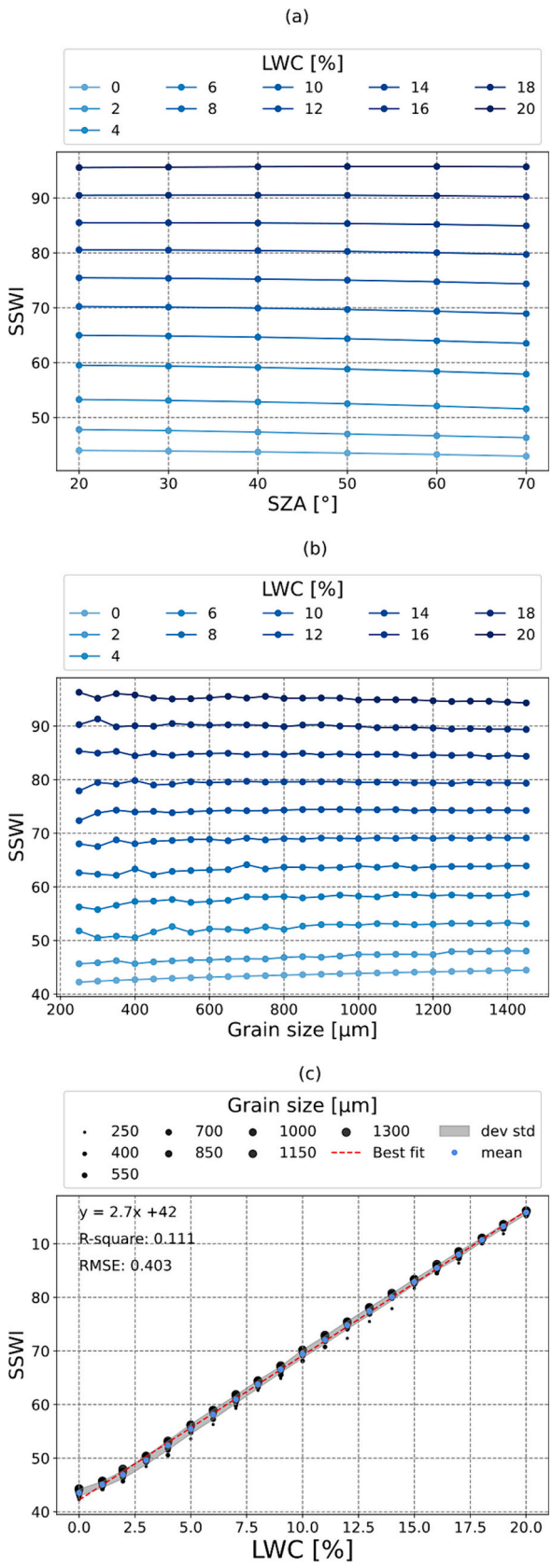

Fig. 5. Sensitivity of simulated SSWI to SZA (a), snow grain size (b), and LWC (c). In (c) the blue dots indicate the mean values, while the gray area represents the standard deviation. The best fit is depicted as a red dashed line. (For interpretation of the references to colour in this figure legend, the reader is referred to the web version of this article.)

The relationship between SSWI and measured LWC is shown in Fig. 7a. Overall, the regression analysis showed an R^2 of 0.8 and an RMSE of 3.3. The modeled LWC was then obtained by inverting the regression model shown in Fig. 7a, according to the following equation:

$$LWC = \frac{SSWI - 38}{1.6} \ [\%] \tag{2}$$

Fig. 7b shows the agreement between modeled LWC (Eq. (2)) and measured LWC using the k-fold cross-validation. The performance of this approach is promising, with an R^2 of 0.7 and a cross-validated error of 3.0%. Overall, the uncertainties can be attributed to the surface anisotropy, topo-atmospheric correction, and PRISMA geolocation errors. In addition, the Snow Sensor describes water status by considering a snowpack thickness and a spatial field of view different from that of reflectance measurements (both SR-3500 and PRISMA data). A recent study demonstrated how the reflectance data can be corrected for topography without the use of a DEM (Carmon et al., 2023), and this may provide interesting perspectives for remote sensing in alpine areas.

In summary, this study provides evidence that LWC can be estimated from remotely sensed data and presents a validation attempt that, to our knowledge, has never been conducted using both field and satellite data.

Finally, the LWC at the surface was mapped from the PRISMA snow cover map by using Eq. (2). Fig. 8a shows a true-colour composite of the PRISMA image over the western European Alps, also including the Laghi Cime Bianche and Plateau Rosa areas. The 9 red points correspond to the in-situ measurements performed with the Snow Sensor at the same time as the PRISMA acquisition. Fig. 8b shows an example of the ATCOR3-derived PRISMA reflectance, with corresponding field-based spectra, before (red dots) and after the smoothing filter (black line), where the absorption feature at 1030 nm and the relative anchor points for the CR analysis are evident. The PRISMA continuum removed spectrum in the 905–1125 nm range is shown at the top of the plot. Fig. 8c shows an LWC map obtained from the PRISMA derived reflectance, while Fig. 8d illustrates the corresponding histogram frequency. The colors are set according to the five classes of Fierz et al. (2009), which are traditionally used to distinguish between dry (0%), moist (0–3%), wet (3–5%), very wet (5–8%), and soaked snow (> 15%). Overall, we found a median of 1.5% for LWC, with a maximum value of 20%. Although the median of the LWC is low, there are also some points above 15%, which can hardly be reached in the few millimeters of the snowpack. LWC is typically limited by the snowpack maximum water holding capacity, which depends on snow grain density and shape. For example, an LWC value of 20% can be too high for densities below 500 kg/m^3, which could never be achieved. However, Quéno et al. (2020) describe scenarios where an impermeable barrier traps meltwater beyond the typical holding capacity. In the superficial layer this could potentially occur under specific circumstances, such as the formation of a sun crust during high solar radiation on cold snow (Fierz et al., 2009), leading to temporarily high LWC in the first few millimeters. When the LWC exceeds about 15%, the snow is classified as slush snow (Fierz et al., 2009), which essentially has very different spectral properties from the wet snow (Di Mauro et al., 2017), probably invalidating the accuracy of BioSNICAR for high LWC. In this work, we focused on seasonal snow, but we acknowledge that on bare ice during the melting season water can stagnate and create supraglacial ponds and bédière. Future research may be focused on the retrieval of liquid water on ice, but in that case, the Snow Sensor probably will not be the optimal instrument for measuring the target variable in the field.

The shaded areas (black areas in Fig. 8d) were excluded from the analysis due to unreliable LWC retrieval. Moreover, patchy snow and heterogeneous pixels can produce erroneous SSWI values and hence inaccurate LWC results. Further research could concentrate on detecting LWC in rugged terrain, mixed pixels, and under vegetation canopies, which are not considered in this study.

Fig. 9 shows the spatial distribution of LWC at the catchment level. We performed a polar plot for each basin, where the angles radiating

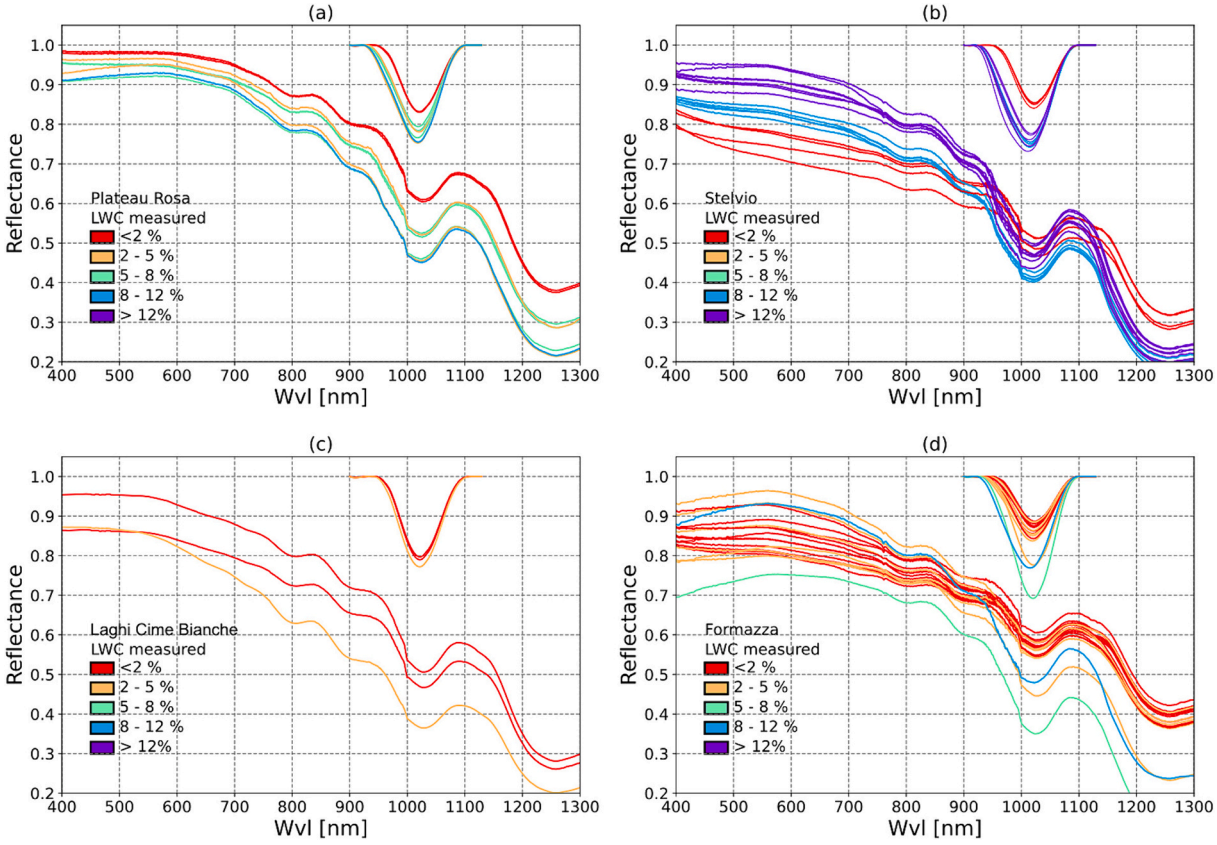

Fig. 6. Measured spectral reflectance (SR-3500) of each campaign site: (a) Plateau Rosa; (b) Stelvio; (c) Laghi Cime Bianche; and (d) Formazza. The continuum removed spectra in the 905–1125 nm range are shown at the top of each plot. Different colors represent the LWC data measured in the field.

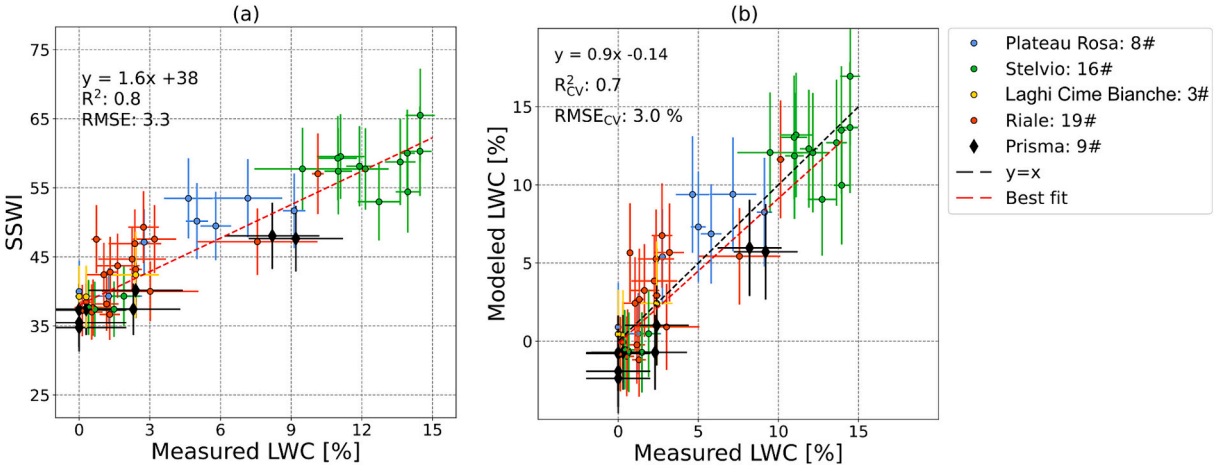

Fig. 7. (a) Relationship between measured LWC and SSWI. Different colors relate to the four field campaigns. The black markers are the PRISMA target pixels. The red dotted line is the best fit between LWC and SSWI. (b) Comparison of the modeled and measured LWC value obtained through the k-fold analysis. (For interpretation of the references to colour in this figure legend, the reader is referred to the web version of this article.)

from the center represent the slope expositions, with 0° corresponding to the North. The distance from the center to each data point represents the elevation, with the center representing lower altitudes, and the outer edges representing higher altitudes. The colour assigned to each data point indicates the amount of LWC. Overall, we found higher LWC values on the southeast-facing (SE) surfaces at different elevations, as highlighted by a dense cluster of blue dots. At higher altitudes, LWC exhibits low values, and above 3500 m we observed LWC = 0% in each catchment. Overall, the results are consistent with those found in the literature (Donahue et al., 2022; Green et al., 2002; Koch et al., 2019; Techel and Pielmeier, 2011). The LWC spatial distribution seems to be consistent with the LWC values found in the campaign conducted during a warm day at 11.00 am, which can lead to such values. However, as expected in the accumulation phase, most of the LWC was found to be equal to zero.

4. Conclusions

In this study, we designed a novel spectral index named SSWI by exploiting the BioSNICAR radiative transfer model. The SSWI was

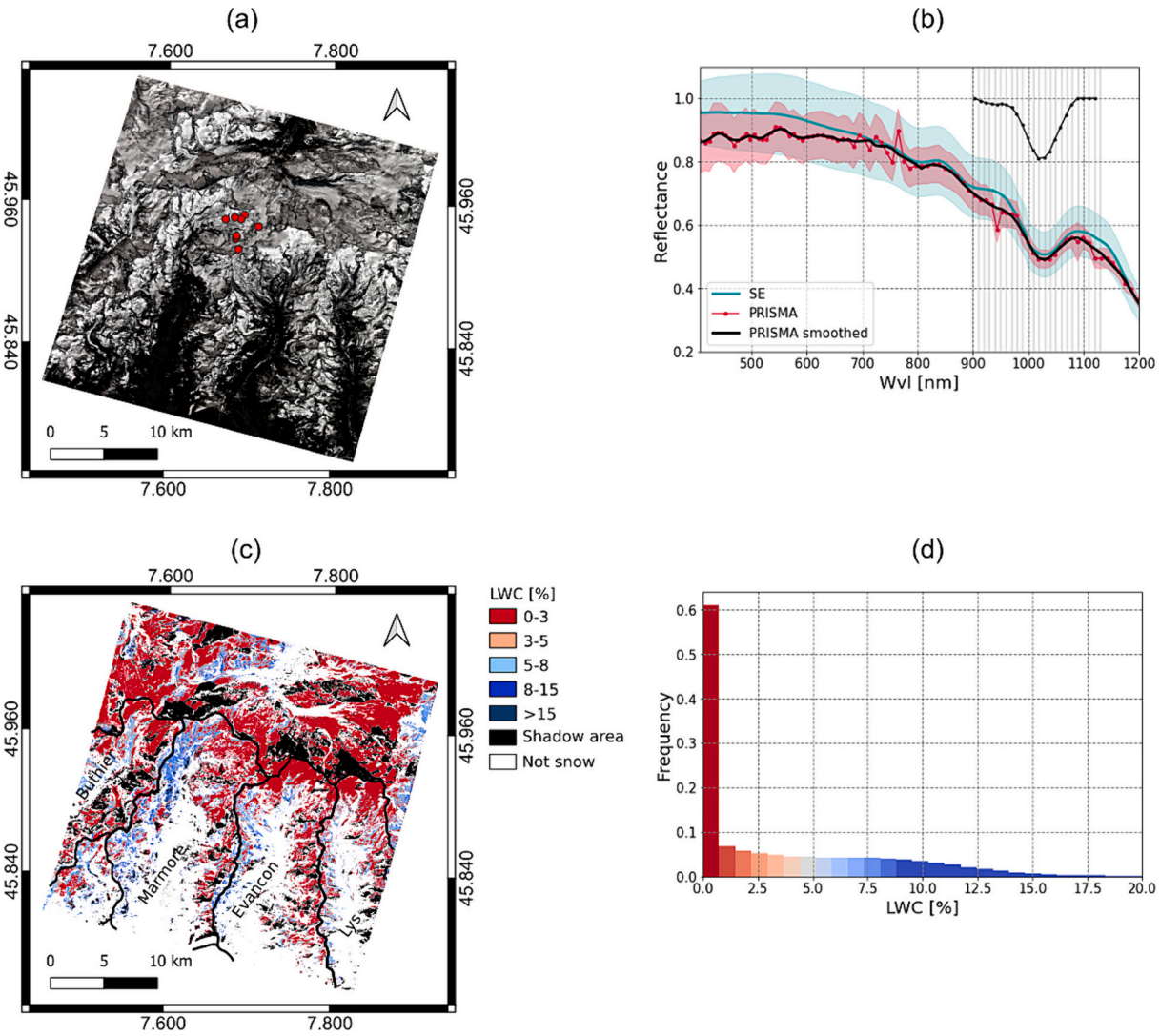

Fig. 8. (a) RGB map of the PRISMA acquisition. The red points are the locations of the ground-based data. (b) Example of PRISMA spectra before (red markers) and after smoothing (black line). The red shaded area indicates the standard deviation of the PRISMA derived reflectance spectra within the 3 × 3 pixel area (centered on the location where the LWC measurements were performed). The turquoise line represents the average of the SR-3500 measurements, and the turquoise shaded area is the standard deviation of the SR-3500 (number of samples = 20). (c) Liquid water content map obtained from PRISMA data. The black lines in Fig. 8c depict four catchments (Buthier, Marmore, Evançon, Lys), as derived from the Aosta Valley DEM. (d) Histogram of the LWC distribution from (c). (For interpretation of the references to colour in this figure legend, the reader is referred to the web version of this article.)

derived from the continuum-removed area of the absorption feature at 1030 nm and normalized to the depth of the absorption at 1025 nm. Using simulated data, we found that this index is sensitive to LWC and uncorrelated both to snow grain size and SZA variation. The index was then tested on data gathered from field spectroscopy and a PRISMA image by using independent field measurements of LWC. The SSWI was used to develop an empirical regression model to infer LWC from hyperspectral data, demonstrating the possibility of mapping surficial liquid water content from space. The model applied to field and PRISMA data allows the estimation of LWC with R^2_{CV} and $RMSE_{CV}$ of 0.7 and 3%, respectively. The LWC map derived from PRISMA data was evaluated in terms of spatial variability in complex topography and we found that higher LWC values occur on South-East facing slopes.

Overall, the correlation between SSWI and LWC highlights the potential of SSWI for quantifying LWC without prior knowledge of grain size, thereby improving our understanding of snowpack dynamics and contributing to improving hydrological models. The SSWI index can be easily computed from hyperspectral data and can be used as an intermediate product to evaluate the spatial and temporal variability of LWC in alpine areas, contributing to the monitoring of the cryosphere. We emphasize the importance of this work in verifying the accuracy of LWC mapping methods through comprehensive validation using field and satellite data. In the absence of field measurements of LWC, the proposed surficial snow water spectral index may be used as a first attempt to qualitatively characterize areas with different spatial LWC patterns. This can help to provide a comprehensive view of the amount and distribution of LWC, having the potential for broader applications at regional scales.

CRediT authorship contribution statement

C. Ravasio: Conceptualization, Methodology, Investigation, Data curation, Writing – original draft. **R. Garzonio:** Conceptualization, Methodology, Data curation, Writing – review & editing. **B. Di Mauro:** Conceptualization, Methodology, Writing – review & editing. **E. Matta:** Methodology, Writing – review & editing. **C. Giardino:** Writing – review & editing. **M. Pepe:** Methodology, Writing – review & editing. **E. Cremonese:** Writing – review & editing. **P. Pogliotti:** Writing – review &

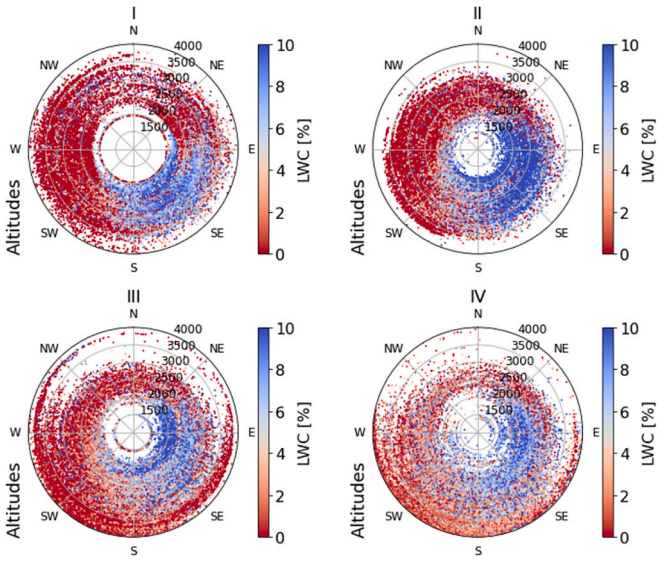

Fig. 9. Polar plots of LWC distribution in relation to the slope exposition (theta) and elevation (radius) in the four investigated catchments.

editing. **C. Marin:** Writing – review & editing. **R. Colombo:** Conceptualization, Methodology, Investigation, Data curation, Writing – original draft, Funding acquisition.

Declaration of competing interest

The authors declare that they have no known competing financial interests or personal relationships that could have appeared to influence the work reported in this paper.

Data availability

Data will be made available on request.

Acknowledgements

This work has been supported by the SCIA (Sviluppo di algoritmi per lo studio della Criosfera mediante Immagini PrismA) and the CRIOSAR (Applicazioni SAR multifrequenza alla criosfera) project, both funded by the Italian Space Agency (ASI). We greatly acknowledge the Italian Space Agency and A. Montuori (ASI) for the discussion during the projects. We acknowledge G. Bramati (UZH), G. Pozzi, and G. Tagliabue for their help in the field data collection.

We would like to thank the anonymous reviewers for their useful comments and suggestions.

References

Awasthi, S., Varade, D., Kumar Thakur, P., Kumar, A., Singh, H., Jain, K., Snehmani, 2022. Development of a novel approach for snow wetness estimation using hybrid polarimetric RISAT-1 SAR datasets in North-Western Himalayan region. J. Hydrol. 612, 128252 https://doi.org/10.1016/j.jhydrol.2022.128252.

Bohn, N., Guanter, L., Kuester, T., Preusker, R., Segl, K., 2020. Coupled retrieval of the three phases of water from spaceborne imaging spectroscopy measurements. Remote Sens. Environ. 242, 111708 https://doi.org/10.1016/j.rse.2020.111708.

Bohn, N., Painter, T.H., Thompson, D.R., Carmon, N., Susiluoto, J., Turmon, M.J., Helmlinger, M.C., Green, R.O., Cook, J.M., Guanter, L., 2021. Optimal estimation of snow and ice surface parameters from imaging spectroscopy measurements. Remote Sens. Environ. 264, 112613 https://doi.org/10.1016/j.rse.2021.112613.

Bohn, N., Di Mauro, B., Colombo, R., Thompson, D.R., Susiluoto, J., Carmon, N., Turmon, M.J., Guanter, L., 2022. Glacier ice surface properties in South-West Greenland ice sheet: first estimates from PRISMA imaging spectroscopy data. J. Geophys. Res. Biogeosci. 127, 1–21. https://doi.org/10.1029/2021JG006718.

Boyne, H.S., Fisk, D., 1987. A comparison of snow cover liquid water measurement techniques. Water Resour. Res. 23 (10), 1833–1836.

Brun, E., Martin, E., Simon, V., Gendre, C., Coleou, C., 1989. An energy and mass model of snow cover suitable for operational avalanche forecasting. J. Glaciol. 35 (121), 333–342.

Busetto, L., Ranghetti, L., 2020. prismaread: A tool for facilitating access and analysis of prisma l1/l2 hyperspectral imagery. URL. https://lbusett.github.io/prismaread/.

Carmon, N., Berk, A., Bohn, N., Brodrick, P.G., Dozier, J., Johnson, M., Miller, C.E., Thompson, D.R., Turmon, M., Bachmann, C.M., Green, R.O., Eckert, R., Liggett, E., Nguyen, H., Ochoa, F., Okin, G.S., Samuels, R., Schimel, D., Song, J.J., Susiluoto, J., 2023. Shape from spectra. Remote Sens. Environ. 288, 113497 https://doi.org/10.1016/j.rse.2023.113497.

Casey, K.A., Kääb, A., Benn, D.I., 2012. Geochemical characterization of supraglacial debris via in situ and optical remote sensing methods: a case study in Khumbu Himalaya, Nepal. Cryosphere 6, 85–100. https://doi.org/10.5194/tc-6-85-2012.

Chevrollier, L.-A., Cook, J.M., Halbach, L., Jakobsen, H., Benning, L.G., Anesio, A.M., Tranter, M., 2022. Light absorption and albedo reduction by pigmented microalgae on snow and ice. J. Glaciol. X, 1–9. https://doi.org/10.1017/jog.2022.64.

Clark, R.N., Roush, T.L., 1984. Reflectance spectroscopy: Quantitative analysis techniques for remote sensing applications. J. Geophys. Res. Solid Earth 89 (B7), 6329–6340.

Colbeck, S.C., 1980. Thermodynamics of snow metamorphism due to variations in curvature. J. Glaciol. 26, 291–301. https://doi.org/10.3189/s0022143000010832.

Colombo, R., Garzonio, R., Di Mauro, B., Dumont, M., Tuzet, F., Cogliati, S., Pozzi, G., Maltese, A., Cremonese, E., 2019. Introducing thermal inertia for monitoring snowmelt processes with remote sensing. Geophys. Res. Lett. 46, 4308–4319. https://doi.org/10.1029/2019GL082193.

Conway, H., Raymond, C.F., 1993. Snow stability during rain. J. Glaciol. 39 (133), 635–642.

Cook, J.M., Tedstone, A.J., Williamson, C., McCutcheon, J., Hodson, A.J., Dayal, A., Skiles, M., Hofer, S., Bryant, R., Mcaree, O., Mcgonigle, A., 2020. Glacier algae accelerate melt rates on the South-Western Greenland ice sheet. Cryosphere 14 (1), 309–330.

Di Mauro, B., Cogliati, S., Bohn, N., Traversa, G., Garzonio, R., Tagliabue, G., Bramati, G., Cremonese, E., Julitta, T., Kokhanovsky, A., Giardino, C., Panigada, C., 2024. Evaluation of PRISMA products over snow in the Alps and Antarctica. Earth and Space Science 11, e2023EA003482. https://doi.org/10.1029/2023EA003482.

Di Mauro, B., Baccolo, G., Garzonio, R., Giardino, C., Massabò, D., Piazzalunga, A., Rossini, M., Colombo, R., 2017. Impact of impurities and cryoconite on the optical properties of the Morteratsch glacier (Swiss Alps). Cryosphere 11, 2393–2409. https://doi.org/10.5194/tc-11-2393-2017.

Di Mauro, B., Garzonio, R., Baccolo, G., Gilardoni, S., Rossini, M., Colombo, R., 2021. Light-absorbing particles in snow and ice: a brief journey across latitudes. In: Springer Series in Light Scattering: Volume 7: Light Absorption and Scattering in Turbid Media, pp. 1–29. https://doi.org/10.1007/978-3-030-87683-8_1.

Di Mauro, B., Garzonio, R., Ravasio, C., Orlandi, V., Baccolo, G., Gilardoni, S., Remias, D., Leoni, B., Rossini, M., Colombo, R., 2024. Combined effect of algae and dust on snow spectral and broadband albedo. J. Quant. Spectrosc. Radiat. Transf. 316, 108906 https://doi.org/10.1016/j.jqsrt.2024.108906.

Dingman, S.L., 2015. Physical Hydrology. Waveland press.

Donahue, C., Skiles, S.M., Hammonds, K., 2022. Mapping liquid water content in snow at the millimeter scale: an intercomparison of mixed-phase optical property models using hyperspectral imaging and in situ measurements. Cryosphere 16 (1), 43–59. https://doi.org/10.5194/tc-16-43-2022.

Donahue, C.P., Menounos, B., Viner, N., Skiles, S.M., Beffort, S., Denouden, T., Arriola, S. G., White, R., Heathfield, D., 2023. Bridging the gap between airborne and spaceborne imaging spectroscopy for mountain glacier surface property retrievals. Remote Sens. Environ. 299, 113849 https://doi.org/10.1016/j.rse.2023.113849.

Dozier, J., 1989. Spectral signature of alpine snow cover from the Landsat thematic mapper. Remote Sens. Environ. 28, 9–22. https://doi.org/10.1016/0034-4257(89)90101-6.

Dozier, J., Painter, T.H., 2004. Multispectral and hyperspectral remote sensing of alpine snow properties. Annu. Rev. Earth Planet. Sci. 32, 465–494. https://doi.org/10.1146/annurev.earth.32.101802.120404.

Dumont, M., Arnaud, L., Picard, G., Libois, Q., Lejeune, Y., Nabat, P., Voisin, D., Morin, S., 2017. In situ continuous visible and near-infrared spectroscopy of an alpine snowpack. Cryosphere 11 (3), 1091–1110. https://doi.org/10.5194/tc-11-1091-2017.

Engstrom, C.B., Williamson, S.N., Gamon, J.A., Quarmby, L.M., 2022. Seasonal development and radiative forcing of red snow algal blooms on two glaciers in British Columbia, Canada, summer 2020. Remote Sens. Environ. 280, 113164 https://doi.org/10.1016/j.rse.2022.113164.

Fierz, C., Armstrong, R.L., Durand, Y., Etchevers, P., Greene, E., McClung, D.M., Nishimura, K., Satayawali, P.K., Sokratov, S.A., 2009. The international classification for seasonal snow on the ground. In: IHP-VII Tech. Doc. Hydrol. N°83, IACS Contrib. N°1 83.

Fisk, D., 1986. Method of measuring liquid water mass fraction of snow by alcohol solution. J. Glaciol. 32 (112), 538–539.

Flanner, M.G., Zender, C.S., Randerson, J.T., Rasch, P.J., 2007. Present-day climate forcing and response from black carbon in snow. J. Geophys. Res. Atmos. 112 (D11) https://doi.org/10.1029/2006JD008003.

Flanner, M.G., Arnheim, J.B., Cook, J.M., Dang, C., He, C., Huang, X., Singh, D., Skiles, S. M.K., Whicker, C.A., Zender, C.S., 2021. SNICAR-ADv3: a community tool for modeling spectral snow albedo. Geosci. Model Dev. 14 (12), 7673–7704. https://doi.org/10.5194/gmd-14-7673-2021.

FPGA Company, 2018. Slf Snow Sensor – User Manual. Available at. https://fpga-company.com/wp-content/uploads/2018/10/SLFSnowSensor-User-Manual-Version-1.3.pdf.

Garzonio, R., Di Mauro, B., Cogliati, S., Rossini, M., Panigada, C., Delmonte, B., Maggi, V., Colombo, R., 2018. A novel hyperspectral system for high resolution imaging of ice cores: application to light-absorbing impurities and ice structure. Cold Reg. Sci. Technol. 155, 47–57. https://doi.org/10.1016/j.coldregions.2018.07.005.

Green, R.O., Dozier, J., Roberts, D., Painter, T., 2002. Spectral snow-reflectance models for grain-size and liquid-water fraction in melting snow for the solar-reflected spectrum. Ann. Glaciol. 34, 71–73. https://doi.org/10.3189/172756402781817987.

Green, R.O., Painter, T.H., Roberts, D.A., Dozier, J., 2006. Measuring the expressed abundance of the three phases of water with an imaging spectrometer over melting snow. Water Resour. Res. 42 https://doi.org/10.1029/2005WR004509.

Hall, D.K., Riggs, G.A., 1995. Mapping global snow cover using moderate resolution imaging spectroradiometer (MODIS) data. Glaciol. Data 33, 13–17.

Houtz, D., Naderpour, R., Schwank, M., Steffen, K., 2019. Snow wetness and density retrieved from L-band satellite radiometer observations over a site in the West Greenland ablation zone. Remote Sens. Environ. 235, 111361 https://doi.org/10.1016/j.rse.2019.111361.

Jones, E.B., Rango, A., Howell, S.M., 1983. Snowpack liquid water determinations using freezing calorimetry. Hydrol. Res. 14 (3), 113–126.

Kattelmann, R., Dozier, J., 1999. Observations of snowpack ripening in the Sierra Nevada, California, USA. J. Glaciol. 45 (151), 409–416.

Kawashima, K., Endo, T., Takeuchi, Y., 1998. A portable calorimeter for measuring liquid-water content of wet snow. Ann. Glaciol. 26, 103–106.

Koch, F., Henkel, P., Appel, F., Schmid, L., Bach, H., Lamm, M., Prasch, M., Schweizer, J., Mauser, W., 2019. Retrieval of snow water equivalent, liquid water content, and snow height of dry and wet snow by combining GPS signal attenuation and time delay. Water Resour. Res. 55, 4465–4487. https://doi.org/10.1029/2018WR024431.

Kokhanovsky, A., Lamare, M., Danne, O., Brockmann, C., Dumont, M., Picard, G., Arnaud, L., Favier, V., Jourdain, B., Meur, E.L., Di Mauro, B., Aoki, T., Niwano, M., Rozanov, V., Korkin, S., Kipfstuhl, S., Freitag, J., Hoerhold, M., Zuhr, A., Vladimirova, D., Faber, A.K., Steen-Larsen, H.C., Wahl, S., Andersen, J.K., Vandecrux, B., van As, D., Mankoff, K.D., Kern, M., Zege, E., Box, J.E., 2019. Retrieval of snow properties from the Sentinel-3 ocean and land colour instrument. Remote Sens. 11 (19), 2280. https://doi.org/10.3390/rs11192280.

Kokhanovsky, A., Di Mauro, B., Colombo, R., 2022. Snow surface properties derived from PRISMA satellite data over the Nansen ice shelf (East Antarctica). Front. Environ. Sci. 1420. https://doi.org/10.3389/fenvs.2022.904585.

Kokhanovsky, A.A., Brell, M., Segl, K., Bianchini, G., Lanconelli, C., Lupi, A., Petkov, B., Picard, G., Arnaud, L., Stone, R.S., Chabrillat, S., 2023. First retrievals of surface and atmospheric properties using EnMAP measurements over Antarctica. Remote Sens. 15 (12), 304. https://doi.org/10.3390/rs15123042.

Lundberg, A., 1997. Laboratory calibration of TDR-probes for snow wetness measurements. Cold Reg. Sci. Technol. 25 (3), 197–205.

Ma, W., Xiao, P., Zhang, X., Song, Y., Ma, T., Ye, L., 2020. Retrieving snow wetness based on surface and volume scattering simulation. ISPRS J. Photogramm. Remote Sens. 169, 17–28. https://doi.org/10.1016/j.isprsjprs.2020.08.021.

Mazurkiewicz, A.B., Callery, D.G., J, J.J, 2008. Assessing the controls of the snow energy balance and water available for runoff in a rain-on-snow environment. J. Hydrol. 354 (1–4), 1–14. https://doi.org/10.1016/j.jhydrol.2007.12.027.

Naegeli, K., Damm, A., Huss, M., Schaepman, M., Hoelzle, M., 2015. Imaging spectroscopy to assess the composition of ice surface materials and their impact on glacier mass balance. Remote Sens. Environ. 168, 388–402. https://doi.org/10.1016/j.rse.2015.07.006.

Negi, H.S., Kokhanovsky, A., 2011. Retrieval of snow albedo and grain size using reflectance measurements in Himalayan basin. Cryosphere 5 (1), 203–217. https://doi.org/10.5194/tc-5-203-2011.

Negi, H.S., Jassar, H.S., Saravana, G., Thakur, N.K., Snehmani, Ganju, A., 2013. Snow-cover characteristics using Hyperion data for the Himalayan region. Int. J. Remote Sens. 34 (6), 2140–2160. https://doi.org/10.1080/01431161.2012.742213.

Nolin, A.W., Dozier, J., 2000. A hyperspectral method for remotely sensing the grain size of snow. Remote Sens. Environ. 74 (2), 207–216. https://doi.org/10.1016/S0034-4257(00)00111-5.

Painter, T.H., Seidel, F.C., Bryant, A.C., McKenzie Skiles, S., Rittger, K., 2013. Imaging spectroscopy of albedo and radiative forcing by light-absorbing impurities in mountain snow. J. Geophys. Res. Atmos. 118, 9511–9523. https://doi.org/10.1002/jgrd.50520.

Pepe, M., Pompilio, L., Ranghetti, L., Nutini, F., Boschetti, M., 2023. Mapping spatial distribution of crop residues using PRISMA satellite imaging spectroscopy. Eur. J. Remote Sens. 56 (1), 1–16. https://doi.org/10.1080/22797254.2022.2122872, 2122.

Picard, G., Libois, Q., Arnaud, L., 2016. Refinement of the ice absorption spectrum in the visible using radiance profile measurements in Antarctic snow. Cryosphere 10 (6), 2655–2672. https://doi.org/10.5194/tc-2016-146.

Quéno, L., Fierz, C., Van Herwijnen, A., Longridge, D., Wever, N., 2020. Deep ice layer formation in an alpine snowpack: monitoring and modeling. Cryosphere 14, 3449–3464. https://doi.org/10.5194/tc-14-3449-2020.

Richter, R., 1998. Correction of satellite imagery over mountainous terrain. Applied optics 37 (18), 4004–4015.

Schaepman-Strub, G., Schaepman, M.E., Painter, T.H., Dangel, S., Martonchik, J.V., 2006. Reflectance quantities in optical remote sensing-definitions and case studies. Remote Sens. Environ. 103 (1), 27–42. https://doi.org/10.1016/j.rse.2006.03.002.

Scheffler, D., Hollstein, A., Diedrich, H., Segl, K., Hostert, P., 2017. AROSICS: An automated and robust open-source image co-registration software for multi-sensor satellite data. Remote sensing 9 (7), 676.

Schläpfer, D., Borel, C.C., Keller, J., Itten, K.I., 1998. Atmospheric precorrected differential absorption technique to retrieve columnar water vapor. Remote Sens. Environ. 65, 353–366. https://doi.org/10.1016/S0034-4257(98)00044-3.

Segelstein, D.J., 1981. The Complex Refractive Index of Water. (Doctoral Diss. Univ. Missouri-Kansas City).

Shekhar, C., Srivastava, S., Negi, H.S., Dwivedi, M., 2019. Hyper-spectral data based investigations for snow wetness mapping. Geocarto Int. 34, 664–687. https://doi.org/10.1080/10106049.2018.1438528.

Techel, F., Pielmeier, C., 2011. Point observations of liquid water content in wet snow – investigating methodical, spatial and temporal aspects. Cryosphere 5, 405–418. https://doi.org/10.5194/tc-5-405-2011.

Thompson, D.R., Green, R.O., Bradley, C., Brodrick, P.G., Mahowald, N., Dor, E. Ben, Bennett, M., Bernas, M., Carmon, N., Chadwick, K.D., Clark, R.N., Coleman, R.W., Cox, E., Diaz, E., Eastwood, M.L., Eckert, R., Ehlmann, B.L., Ginoux, P., Ageitos, M. G., Grant, K., Guanter, L., Pearlshtien, D.H., Helmlinger, M., Herzog, H., Hoefen, T., Huang, Y., Keebler, A., Kalashnikova, O., Keymeulen, D., Kokaly, R., Klose, M., Li, L., Lundeen, S.R., Meyer, J., Middleton, E., Miller, R.L., Mouroulis, P., Oaida, B., Obiso, V., Ochoa, F., Olson-Duvall, W., Okin, G.S., Painter, T.H., Pérez García-Pando, C., Pollock, R., Realmuto, V., Shaw, L., Sullivan, P., Swayze, G., Thingvold, E., Thorpe, A.K., Vannan, S., Villarreal, C., Ung, C., Wilson, D.W., Zandbergen, S., 2024. On-orbit calibration and performance of the EMIT imaging spectrometer. Remote Sens. Environ. 303 https://doi.org/10.1016/j.rse.2023.113986.

Warren, S.G., 1982. Optical properties of snow. Rev. Geophys. 20 (1), 67–89. https://doi.org/10.1029/RG020i001p00067.

Warren, S.G., Brandt, R.E., 2008. Optical constants of ice from the ultraviolet to the microwave: a revised compilation. J. Geophys. Res. 113, D14. https://doi.org/10.1029/2007JD009744.

Williams, M.W., Erickson, T.A., Petrzelka, J.L., 2010. Visualizing meltwater flow through snow at the centimetre-to-metre scale using a snow guillotine. Hydrol. Process. 24 (15), 2098–2110. https://doi.org/10.1002/hyp.7630.

Wiscombe, W.J., Warren, S.G., 1980. A model for the spectral albedo of snow. I: pure snow. J. Atmos. Sci. 37 (12), 2712–2733.